

# Star formation in the Vela Molecular Clouds

## III. Near IR images and mm photometry of D-cloud IRAS sources<sup>\*,\*\*</sup>

F. Massi<sup>1,2</sup>, T. Giannini<sup>1,2,3</sup>, D. Lorenzetti<sup>2,3</sup>, R. Liseau<sup>4</sup>, A. Moneti<sup>5</sup>, and P. Andreani<sup>6</sup>

<sup>1</sup> Istituto Astronomico, Università “La Sapienza”, Via Lancisi 29, I-00161 Rome, Italy

<sup>2</sup> Osservatorio Astronomico di Roma, Via Frascati 33, I-00040 Monte Porzio (Rome), Italy

<sup>3</sup> Istituto di Fisica dello Spazio Interplanetario - CNR, Casella Postale 27, I-00044 Frascati (Rome), Italy

<sup>4</sup> Stockholm Observatory, S-133 36 Saltsjöbaden, Sweden

<sup>5</sup> ISO Science Operation Centre, Astrophysics Division of ESA, Box 50727, E-28080 Madrid, Spain

<sup>6</sup> Dipartimento di Astronomia - Università di Padova, V.lo dell’Osservatorio 5, I-35122 Padova, Italy

Received July 17, 1998; accepted January 28, 1999

**Abstract.** We present the first results of a sensitive ( $K \approx 17$  mag) near IR ( $JHK$ ) imaging survey of a complete IRAS selected sample of Young Stellar Objects (YSO’s) belonging to a Giant Molecular Cloud (GMC) located in the Vela Molecular Ridge (VMR). We provide accurate position and photometry for more than 1300 sources, along with the identification of possible NIR counterparts of the IRAS objects. Through near infrared and 1.3 mm photometry we have determined the spectral energy distributions of 11 newly discovered Class I sources and possibly one Herbig Ae/Be star. Their bolometric luminosities indicate that they are protostellar objects of intermediate masses ( $\leq 10 M_{\odot}$ ) with envelopes containing a not negligible fraction of the central condensed matter. Many sources are associated to diffuse emission which hosts multiple systems of point-like objects. Although clustering is well evident, the NIR counterparts of the IRAS sources seem to be single objects and quite often there are more than one source in the field with  $JHK$  colours typical of Class I objects. These findings support the fact that in VMR, as well, stars of different masses are sharing the same birthplace.

**Key words:** stars: formation — stars: pre-main sequence — infrared: stars — ISM: individual objects (Vela clouds)

## 1. Introduction

One of the critical issues of star formation is to understand how the evolution of molecular clouds is interrelated to the birth of new stars within them. The current theoretical picture of these early stages is affected by large uncertainties, but some of them can be effectively circumvented by means of dedicated observations aiming to separate the effects of the different variables as much as possible.

Obvious observational constraints have biased so far the selection of targets towards clouds of relatively low mass ( $M < 10^5 M_{\odot}$ ) located outside the plane of the Galaxy, despite GMC’s lying *in* the plane offer the possibility of studying star formation where the bulk of material actually lies.

Given these motivations, a few years ago we began a multi-frequency study of the young stellar content in the VMR, a complex composed of four different molecular clouds (with molecular masses of  $10^5 \div 10^6 M_{\odot}$ ) which have been actively forming stars (May et al. 1988; Murphy & May 1991). The Vela Molecular Ridge offers some advantages to the observer: it is possible to study 4 different GMC’s with the same methods, so as to derive properties of YSO’s which are affected by the same environmental and observational effects; it allows to investigate star formation in the outer Galaxy minimizing the problems due to confusion; the region is expected to be relatively nearby and it is adjacent to a sky area of equal angular size, void of molecular gas, which constitutes a reference field.

The selection criteria to identify the young objects, the assessment of their cloud membership, and the observational results obtained so far have been communicated in our previous papers (Liseau et al. 1992, and Lorenzetti et al. 1993, hereafter Paper I and Paper II respectively).

Send offprint requests to: F. Massi

\* Based on observations collected at the European Southern Observatory, Chile.

\*\* Table 4 is only available in electronic form at the CDS via anonymous ftp to cdsarc.u-strasbg.fr (130.79.128.5) or via <http://cdsweb.u-strasbg.fr/Abstract.html>

Correspondence to: [massi@coma.mporzio.astro.it](mailto:massi@coma.mporzio.astro.it)

Throughout Papers I and II it was assumed that the infrared emission is dominated by a single object; here we report the first results of an imaging survey aimed to find the near infrared counterparts of the IRAS sources, to extend the spectral energy distributions (SED's) towards short wavelengths, to investigate the source multiplicity and extension. We are also performing a survey of the 1.3 mm continuum emission of IRAS objects in VMR, hence we can complement the near IR imaging data with mm-continuum photometry which allows us both to provide a more accurate determination of the bolometric luminosities and to evaluate the mass of the circumstellar environment around each source.

The details of the observations, data reduction and calibration procedures are described in Sect. 2, while the obtained results are reported in Sect. 3. A short discussion about the present observations is given in Sect. 4, but the reader should refer to a forthcoming paper for a more detailed analysis of the implications of such results.

## 2. Observations and data reduction

### 2.1. Source selection

To study spatial distribution and physical properties of YSO's in relatively close-by molecular clouds, we have selected from our catalogue of observational data (see Papers I and II), based on the IRAS Point Source Catalogue (PSC), the sources obeying the following criteria:

- i)* having passed through all steps described in Papers I and II and being eventually identified as *Class I protostellar candidates*;
- ii)* belonging to the VMR-D cloud (as designated by Murphy & May 1991), which is located at a distance of  $700 \pm 200$  pc from the Sun (Paper I).

Both criteria essentially provide a flux limited sample of 12 IRAS objects with red colours [ $1 \text{ Jy} < F_{12} < F_{25} < F_{60}$ , where  $F_i = F_\nu(i)$  in the IRAS band centred at  $i \mu\text{m}$ ] and associated to molecular gas with a low velocity ( $0 < v_{\text{LSR}} < 14 \text{ km s}^{-1}$ ) compatible with that of the D cloud itself (Murphy & May 1991).

In Table 1 the selected objects are listed along with their equatorial coordinates and the gas velocities detected by means of pointed spectral line observations (CO and/or CS) performed at high spatial resolution (Papers I/II). The identification given in the last column (# IRS) refers to our internal classification and may be useful in order to have a quick reference to the notes on individual sources given elsewhere (Papers I/II). In the Appendix we provide some complementary informations about the sources investigated here. The spatial distribution of the selected sources is depicted in Fig. 1, superimposed on the  $^{12}\text{CO}(1-0)$  integrated intensity contour plot (in galactic

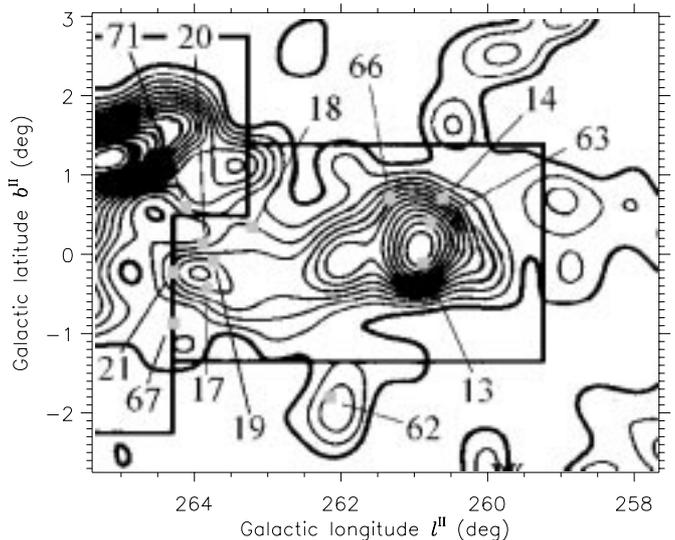


**Fig. 1.** Spatial distribution of the IRAS Class I sources belonging to VMR-D cloud, superimposed on the  $^{12}\text{CO}(1-0)$  integrated intensity map given by Murphy & May (1991). Contour intervals are  $1.3 \text{ K km s}^{-1}$  from  $1.3 \text{ K km s}^{-1}$ ; sources are named according to the internal classification used in Table 1

coordinates) provided by Murphy & May (1991) in their Fig. 5. The selected IRAS sources tend to cluster near the peaks of the molecular emission, namely their original birthplaces, thus giving support to their YSO's nature. Marginal exceptions to this occurrence are represented by IRS 67 and IRS 71 which lie in locations where the integrated intensity is lower; nevertheless we decided to include them for the sake of completeness.

### 2.2. Near-IR imaging

The imaging data were obtained in February 1993 with the IRAC2 near-infrared camera (Moorwood et al. 1992) on the ESO/MPI 2.2 m telescope at La Silla (Chile). The observations were carried out through standard *J* ( $1.25 \mu\text{m}$ ), *H* ( $1.65 \mu\text{m}$ ) and *K* ( $2.20 \mu\text{m}$ ) broad band filters. The  $256 \times 256$  pixels NICMOS3 array was used at a plate scale of  $0.49 \text{ arcsec/pixel}$ , resulting in a field of view of about  $2 \times 2 \text{ arcmin}^2$  on the sky. For each source and for each filter we obtained a set of 3 dithered frames offset from each other by  $30''$  in declination, resulting in total on-source integration times of 120 s, 180 s and 540 s at *J*, *H* and *K*, respectively. The data were reduced through standard IRAF routines and photometry was performed using the DAOPHOT package, in IRAF. Unfortunately, PSF fitting procedures did not work well with our data, so we carried out standard aperture photometry. More details are given in the Appendix.

The *K* brightness of extended sources was obtained by integrating the detected emission down to a  $\sim 5-10\sigma$  level with respect to the underlying background; *J* and *H* brightnesses were derived integrating over the same area.

**Table 1.** Selected IRAS sources

IRAS name	$\alpha(1950.0)$			$\delta(1950.0)$			CO: $v_{\text{LSR}}$ (km s $^{-1}$ )	CS: $v_{\text{LSR}}$ (km s $^{-1}$ )	$F_{1.3 \text{ mm}}$ (mJy)	# IRS
	<i>h</i>	<i>m</i>	<i>s</i>	$^{\circ}$	$'$	$''$				
08328 – 4314	08	32	49.8	–43	14	15	10.2	-	42 $\pm$ 12	62
08375 – 4109	08	37	31.8	–41	09	14	8.4	9.5 <sup>a</sup>	446 $\pm$ 23	13
08393 – 4041	08	39	23.4	–40	41	18	7.5	7.6	529 $\pm$ 27	63
08404 – 4033	08	40	27.0	–40	33	22	6.4	u.l.	38 $\pm$ 12	14
08429 – 4055	08	42	54.4	–40	55	44	-	2.6	-	66
08445 – 4420	08	44	35.6	–44	20	14	4.0/67.9	u.l.	34 $\pm$ 16	67
08448 – 4343	08	44	49.4	–43	43	27	3.9	4.5	1111 $\pm$ 47	17
08470 – 4243	08	47	00.0	–42	43	12	4.3/28.2	-	2510 $\pm$ 116	18
08470 – 4321	08	47	01.3	–43	21	15	12.2	12.2	604 $\pm$ 19	19
08476 – 4306	08	47	39.4	–43	06	01	2.1	2.1 <sup>a</sup>	388 $\pm$ 24	20
08477 – 4359	08	47	47.1	–43	59	34	7.98	2.3/4.5	121 $\pm$ 16	21
08500 – 4254	08	50	01.2	–42	54	11	13.4	-	91 $\pm$ 28	71

<sup>a</sup> Bronfman et al. (1996): see Appendix.

Instrumental magnitudes were converted to absolute values by comparison with ESO photometric standard stars (Bouchet et al. 1989) which also allowed us to check that the zero-points were exceptionally stable during the whole nights (rms variations were  $\sim 0.01 \div 0.03$  mag in  $J$ ,  $H$  and  $K$  bands): the limiting magnitudes of this survey are  $J \approx 18.5$ ,  $H \approx 18.0$  and  $K \approx 17.0$ . Air mass corrections were applied using typical values for the atmospheric extinction coefficients at La Silla ( $E_J = 0.125$ ,  $E_H = 0.080$  and  $E_K = 0.110$  mag/airmass).

A total of  $\approx 1300$  sources have been detected in  $K$ ,  $\approx 1200$  in  $H$  and  $\approx 800$  in  $J$ ; coordinates and magnitudes of all sources found in the  $K$  band are given in Table 4, while the obtained  $JHK$  images are displayed in Fig. 2. For sources undetected in some of the bands, upper limits were estimated in each frame examining the magnitude-error diagrams.

The completeness limit in the  $K$  band is not in principle the same for all frames because of the presence of local nebulosities; however, we obtained the  $K$  luminosity function for each field, which generally shows a turn-off at 15.5 – 16.5 mag (see our forthcoming paper). Thus, we conservatively define as completeness limit the value  $K_{\text{compl}} = 15.5$  mag (i.e. more than one magnitude below the limiting magnitude), which corresponds to complete observations at a  $10\sigma$  detection level.

Some complementary images in the  $L'$  band ( $3.8 \mu\text{m}$ ) were obtained with both the first IRAC  $64 \times 64$  pixels Hg: Cd:Te array at the ESO 2.2 m telescope, and the  $58 \times 62$  pixels InSb array at CTIO during the period 1991-1992. Despite these results are not presented here because of their poor quality, nevertheless we will refer to them in the following, since they help us in the identification of the IRAS counterparts: in fact the sources with an intrinsic IR excess definitely emerge in the  $L'$  band, often remaining the only bright object within the frame area.

### 2.3. NIR positions

Absolute  $\alpha$  and  $\delta$  positions were derived in the observed fields using reference stars whose equatorial coordinates are given in the HST Guide Star Catalogue (GSC). Each  $K$  frame was searched for IR counterparts of GSC stars and the astrometric solution was derived. If a frame contained too few (or none) GSC stars, we first determined the astrometric solution for a Digitized Sky Survey (DSS<sup>1</sup>) plate larger than but including the  $K$  frame field. Then IR counterparts of DSS stars were used to derive the astrometric solution for the  $K$  frame itself. We estimate that the positions given in this paper are accurate within  $1''$  both in RA and DEC.

### 2.4. Millimeter continuum observations

The observations were carried out during September 1992 with the SEST 15 m telescope at La Silla. The antenna fed a  $^3\text{He}$ -cooled bolometer of the MPIfR (Kreysa 1990). The filter set coupled to the atmospheric transmission window provides an effective wavelength around 1.25 mm. The beam size is  $24''$  (HPBW) and the chop throw is  $70''$ .

The sources were located by pointing on a nearby radio quasar with strong millimetric fluxes; the pointing accuracy was most of the time better than  $2''$  and was checked each half an hour.

We observed 11 out of the 12 IRAS sources using integration times  $n \times 200$  s, with  $n$  depending on their expected 1.3 mm intensity, which had been approximately found by extrapolating the IRAS 100  $\mu\text{m}$  flux. The atmospheric transmission was monitored by frequent sky dips.

<sup>1</sup> The Digitized Sky Survey was produced at the Space Telescope Science Institute under U. S. Government grant NAG W-2166. The images of these surveys are based on photographic data obtained using the Oschin Schmidt Telescope on Palomar Mountain and the UK Schmidt Telescope.

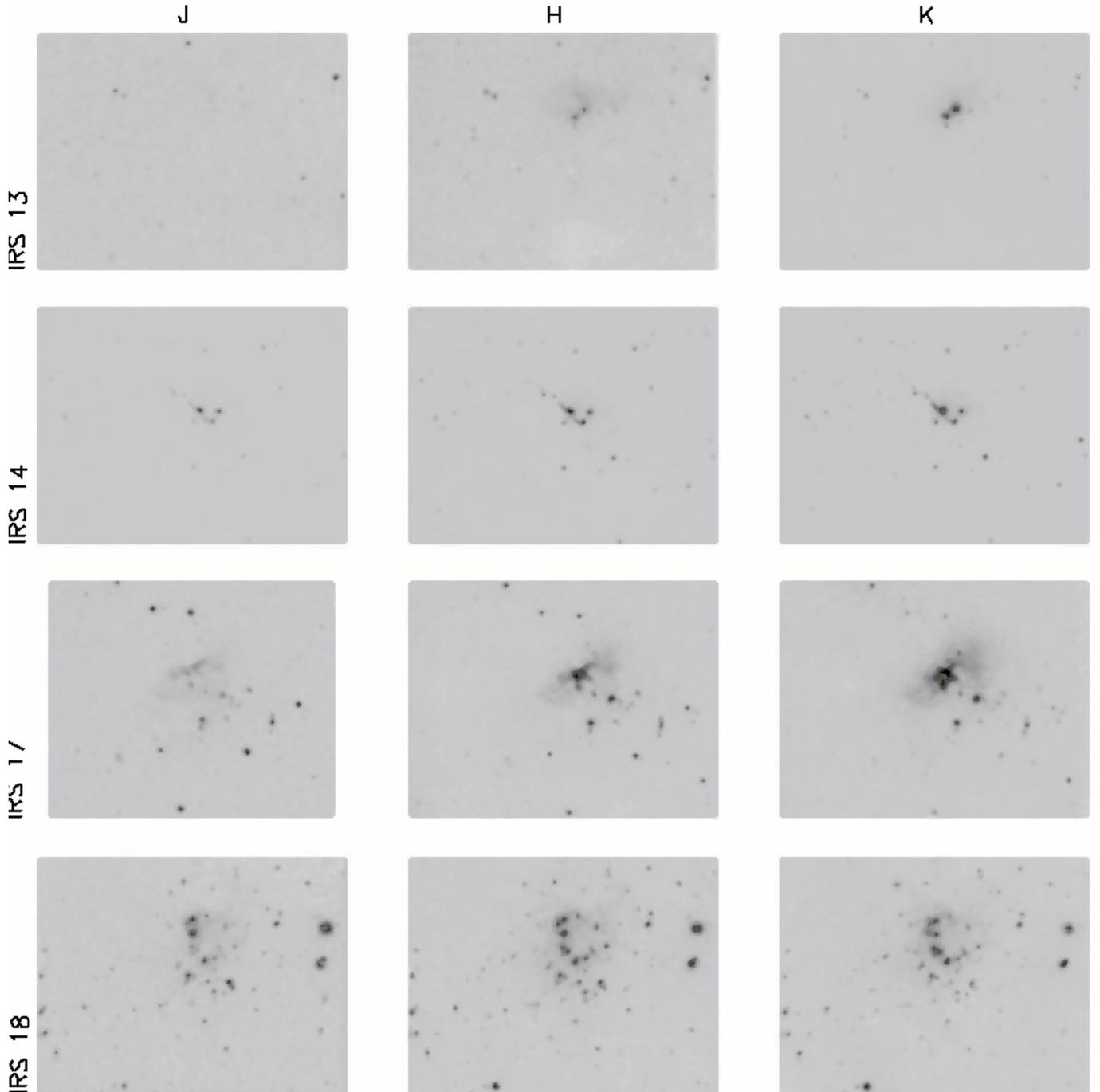


**Fig. 2.** *J*, *H* and *K* images of all observed fields. Each column refers to the same band (indicated above) and each row refers to the same field (indicated on the left-hand side). North is up and east to the left

Uranus, Mars and Saturn were used as primary calibrators and several quasars as secondary calibrators, mainly to detect sky variations during the observations.

The 1.3 mm flux values were corrected for the overall system and atmospheric response through the gain-elevation curve, assuming that the spectra in the millimetric region can be approximated by  $F = F_0(\frac{\nu}{\nu_0})^\alpha$ , where  $\alpha$  is the spectral index of the source. The results of the 1.3 mm photometry are listed in Col. 10 of Table 1 along with their uncertainties.

### 3. Results

#### 3.1. Identifying the NIR counterparts

In order to identify the NIR counterparts of the IRAS sources, we need to determine where the IRAS uncertainty ellipses (which express the position error at a 95% confidence level) lie within each frame. After finding  $\alpha$  and  $\delta$  coordinates as a function of pixel rows and columns for each *K* image (see Sect. 2.3), the IRAS ellipses could be

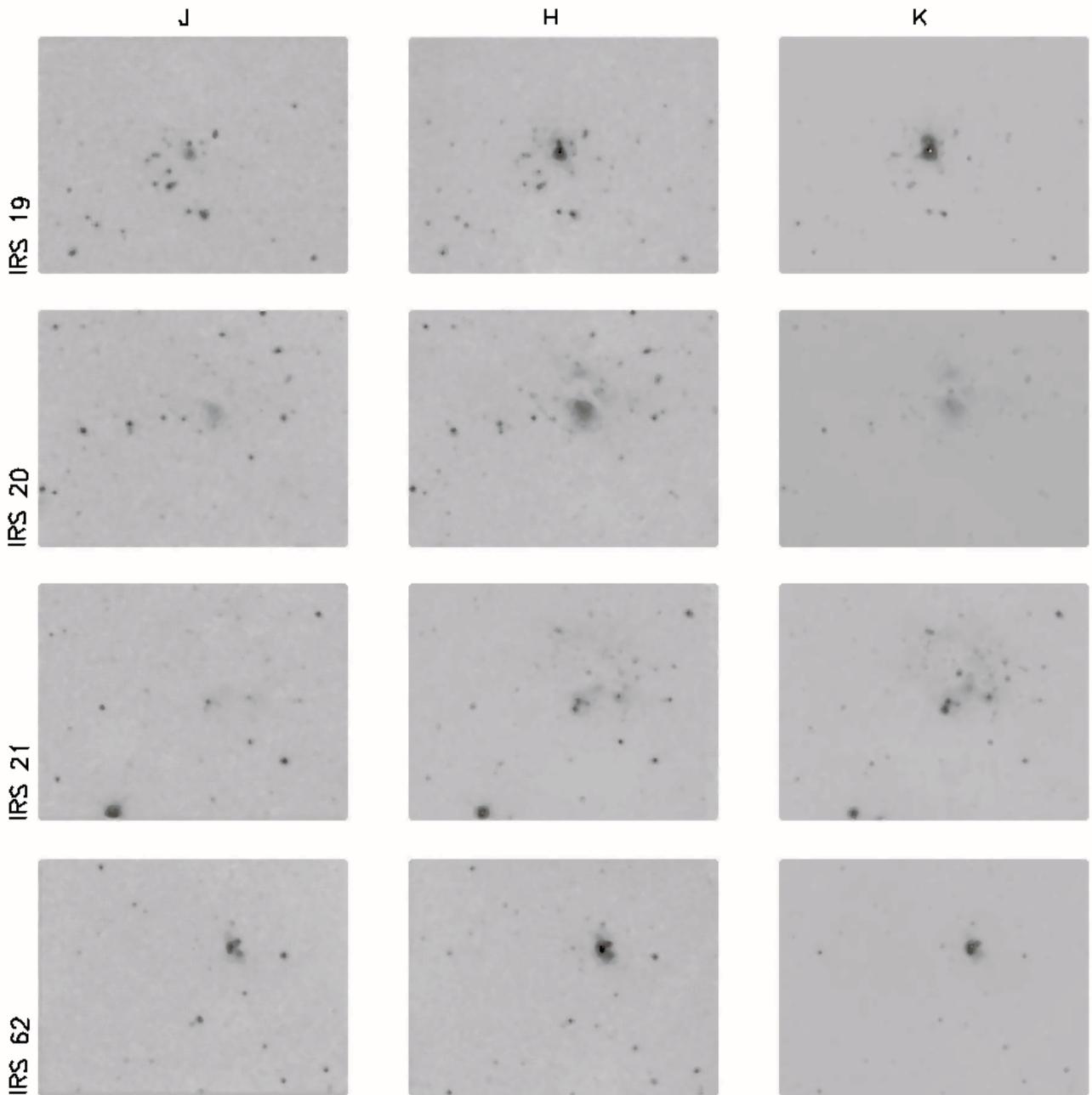


Fig. 2. continued

properly placed on the observed fields. All  $K$  sources within an area of  $\sim 60 \times 60$  arcsec<sup>2</sup> centred on the IRAS ellipse were then examined for finding the best candidates. The NIR counterpart, i.e., the object which effectively contributes the most to the FIR flux, is tentatively selected in each field according to the following criteria:

1. spectral index  $s = d \log(\lambda F_\lambda) / d \log(\lambda) \geq 0$ ;
2. maximum luminosity in the  $K$  band;
3. intrinsic excess in  $(H - K, J - H)$  diagrams (hereafter, we will refer to these simply as colour-colour diagrams);
4. the spectral index  $s$  should be the largest one;
5. closeness to the IRAS ellipse centre.

We noted that sources with spectral indices  $s < 0$  are generally visible in the DSS optical plates, whereas sources with  $s \geq 0$  are not, so item 1 cut off at least bright

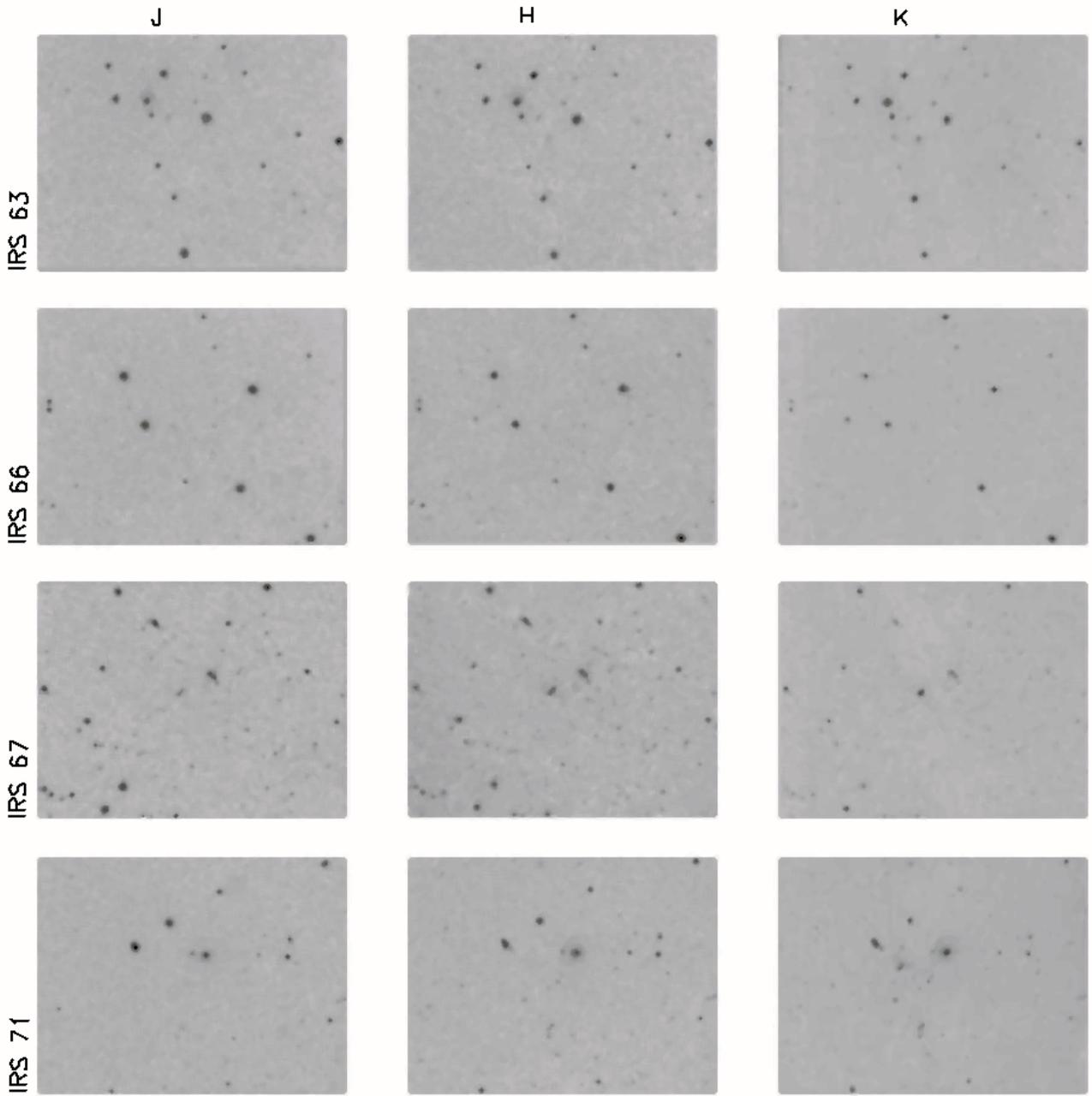


Fig. 2. continued

visible stars. Item 3 should allow to select YSO's, though this criterion can be relaxed since low luminosity Class I sources sometimes do not exhibit IR excesses in colour-colour diagrams and may appear as very reddened stars (see, e.g., Lada & Adams 1992; in the following, we will refer to this paper in analyzing colour-colour diagrams). If the FIR flux was due to a cluster of sources, rather than a single one, we anyway would expect the IRAS uncertainty ellipse to include the location of the cluster (brightness-

weighted) centre. To accurately assess the above requirements, for each field we put all  $K$  sources detected within the  $\sim 60 \times 60$  arcsec<sup>2</sup> area in a  $(H-K, J-H)$  diagram and plotted their SED's in the form of a  $\log(\lambda) - \log(\lambda F_\lambda)$  diagram (see Figs. 3–14, which however report just the SED's of candidate counterparts). This allowed us to rapidly decide which is the NIR counterpart in almost all cases. In the following, we discuss in detail all the observed fields; NIR source numbers refer to those given in Table 4.

### 3.1.1. IRS 13

This field is, at the moment, the only one for which we could not obtain a reliable astrometry; in fact, the DSS plate of the region contains too few stars with a NIR counterpart in the  $K$  frame, confirming that the extinction is large in this area ( $A_V > 30$  mag, as reported in appendix to Paper I). However, the most prominent structure in the field is a reflection nebula (about  $15'' \times 15''$ ) hosting at least 4 point sources (# 22, 25, 27 and 29; see Fig. 3c). Out of these, source # 29 dominates the emission in the  $K$  and  $L'$  bands, and fits the above criteria (see Figs. 3a and c). In the colour-colour diagram (Fig. 3a) it lies in a region typically occupied by luminous Class I sources. Its  $J$ ,  $H$  and  $K$  magnitudes (see Table 4) are equal, within the errors, to those obtained by single channel photometry (given in Paper I). Though this one appears as the main source contributing to the FIR flux, since its  $K$  brightness exceeds that of other sources of about a factor 5 at least, also # 25 has typical colours of Class I sources and # 22 and 27, which were not detected in the  $J$  band, could be protostellar objects of the same type as well. Although, as we will show later, we cannot exclude that such red objects with lower limits at  $J$  may be heavily obscured background stars, it is quite reasonable that all these sources belong to a very young embedded star cluster.

### 3.1.2. IRS 14

The IRAS uncertainty ellipse is roughly centred on a possible reflection nebula hosting a small cluster which contains more stars than reported by West (1980) from optical plates (his designation: ESO 313-N\*10). A single point source, # 37, is by far the brightest object in the  $K$  and  $L'$  bands and, as shown in Fig. 4, is the best candidate to be the NIR counterpart of IRS 14. It clearly exhibits a NIR excess in the colour-colour diagram of Fig. 4a and its  $J$ ,  $H$  and  $K$  magnitudes coincide with those given in Paper I. The colour-colour diagram indicates the presence of other sources with a possible NIR excess in a region that is typically occupied by Classical T-Tauri or Herbig Ae/Be stars; indeed, this means that a more plausible identification for IRS 14 is that it is a Herbig Ae/Be star. Furthermore, both the low mm-continuum flux (see Table 1) and the failing to detect CS(2 – 1) emission (see Paper I) suggest that this region may be more evolved with respect to IRS 13.

### 3.1.3. IRS 17

Again, the IRAS uncertainty ellipse coincides with an extended NIR source, probably a reflection nebula, and is roughly centred on the brightest object (# 57) in the  $K$  and  $L'$  bands, which lies inside the nebula itself. Source

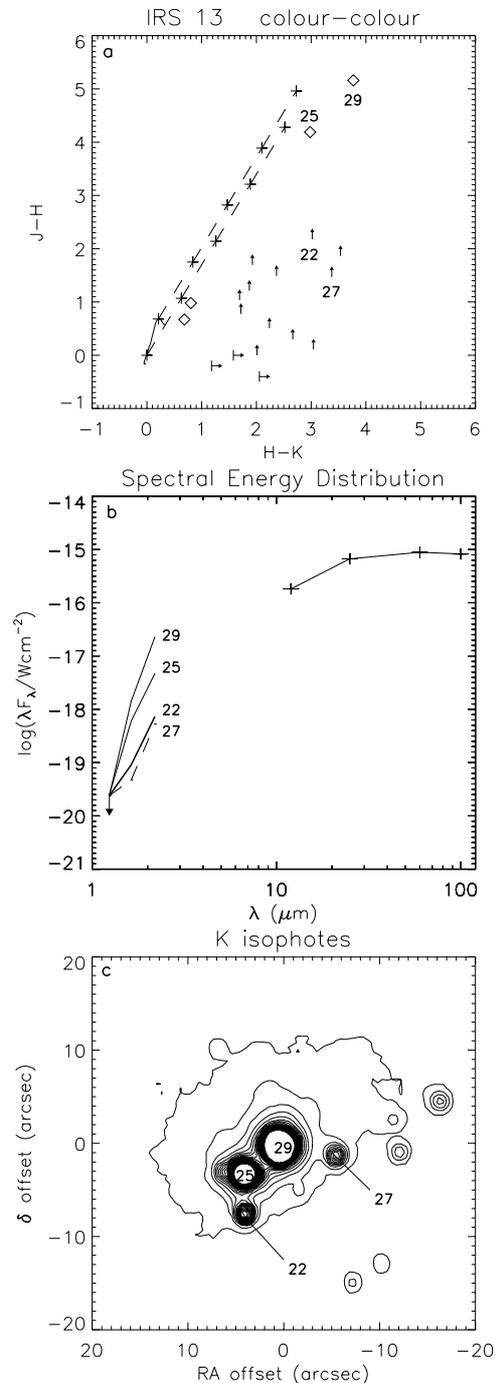


**Fig. 3.** a) Colour-colour diagram, b) SED's of some of the possible NIR counterparts of IRS 13 (along with fluxes in the IRAS bands) and c) contour plot of the  $K$  flux around the IRAS uncertainty ellipse (dotted line). Contours are in steps of  $\sim 1\sigma$  from  $\sim 1\sigma$ . The solid line in the colour-colour diagram marks the locus of main sequence stars (Koornneef 1983), whereas dashed lines are the reddening law according to Rieke & Lebofsky (1985); 10 magnitudes intervals of  $A_V$  are indicated by crosses. Data point on the right of the two dashed lines represent sources with an intrinsic NIR excess. Upward arrows indicate lower limits in  $(J - H)$  and vertical segments with rightward arrows indicate sources with only upper limits at  $J$  and  $H$

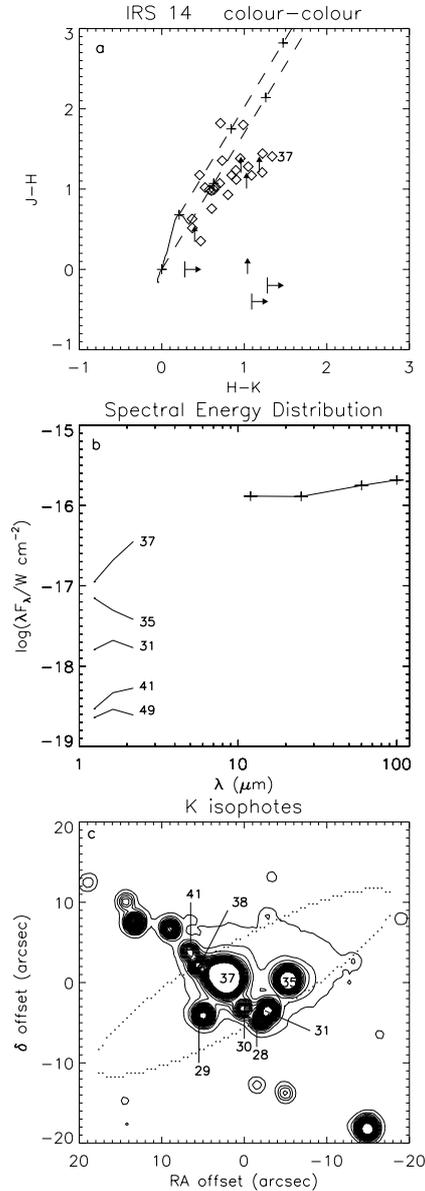


Fig. 4. Same as Fig. 3, but for IRS 14

# 57 has the “right” spectral index (see Fig. 5b) and fulfills the counterpart requirements. Its colours (Fig. 5a) are typical of Class I sources. Our photometry coincides reasonably, within the errors, with the single channel photometry (Paper I). Even if this object is surrounded by other sources satisfying some of the counterpart requirements (# 40, 49, 67, 25; see Fig. 5b), these are fainter, with the brightest ones essentially located to the south and south-west of the ellipse and not symmetrically arranged around it; thus # 57 appears as the main source of FIR flux. However, we note that # 40, an object with a NIR excess and also detected in the  $L'$  band, has a  $K$  flux which is only a factor of 2 less than that of #57. Its protostellar nature is confirmed by NIR images in a narrow band centred at the  $\text{H}_2 v = 1-0 \text{ S}(1)$  line ( $2.12 \mu\text{m}$ ) show-

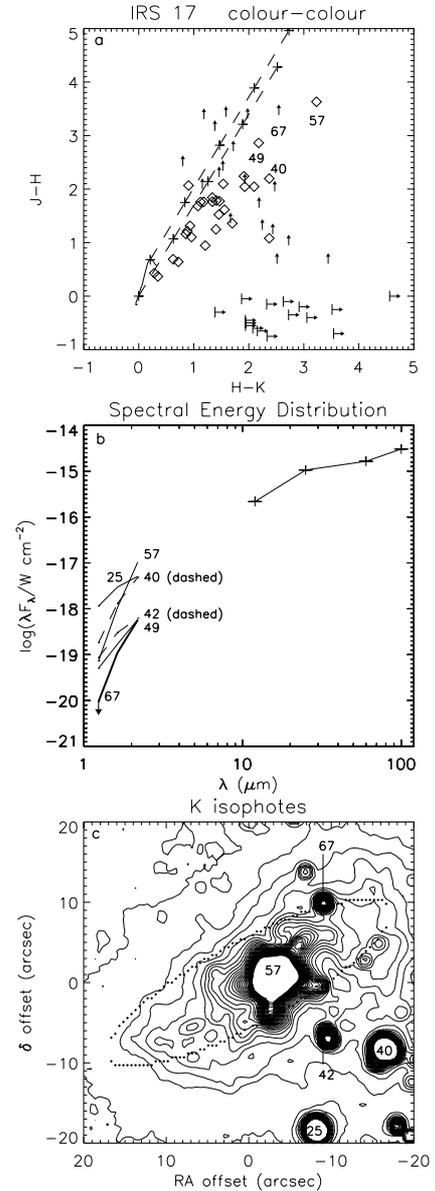


Fig. 5. Same as Fig. 3, but for IRS 17

ing a jet which appears to be driven by the source (Massi et al. 1997). The colour-colour diagram indicates the presence of other sources with NIR excesses and colours typical of classical T-Tauri stars, Herbig Ae/Be stars and Class I sources, suggesting this field is an extremely young embedded star cluster.

#### 3.1.4. IRS 18

The best NIR counterpart candidate, as shown in Fig. 6, is source # 119, which lies at the margin of the uncertainty ellipse and has the greatest spectral index. Our photometry indicates that the previously found NIR source (Paper I), corresponding to our # 137, must be discarded because of both its negative spectral index (see Fig. 6b)

and its lack of a NIR intrinsic excess (see Fig. 6a). In fact, according to Fig. 6a its colours are more or less compatible with those of a reddened A0 V star. Source # 138, which lies towards the north-eastern edge of the ellipse, and source # 121, located within the ellipse, also fulfil some of the counterpart criteria and could contribute to the FIR emission (as suggested by the location of the IRAS ellipse, straddling # 119, # 121 and # 138), though their  $K$  fluxes are 3.5 and 5.5 times less than that of # 119, respectively. We note the presence of another object (# 176) with possible colours of a luminous Class I source (its  $J$  magnitude is a lower limit), even brighter than # 119 in  $K$ , but lying  $\sim 30''$  north-east of the IRAS ellipse centre, then probably unrelated to the bulk of FIR flux. No images in the  $L'$  band are available.

It is interesting to note that the presence of main sequence stars just towards IRS 18 (source # 137) may serve to constrain the distance to the region. As said,  $JHK$  colours indicate that # 137 may be an A0 V star with negligible extinction; since the GSC reports a star with  $V = 12.38$  mag in the same position, this confirms that the identification is roughly correct and that an A0 V star with intrinsic brightness  $V \sim 10.8$  mag and  $A_V \sim 1.5$  mag could account for the  $VJHK$  magnitudes. Allen (1976) quotes an absolute magnitude  $V = 0.7$  for an A0 V star, hence source # 137 results to be located at a distance of  $\sim 1000$  pc. We can exclude a supergiant star since a B7 I, which has roughly the same  $VJHK$  colours as an A0 V (Koornneef 1983), would lie at a distance  $> 16000$  pc (which is much more than we can reasonably assume for the VMR; see Paper I). Considering a mean extinction gradient of  $1.9$  mag  $\text{kpc}^{-1}$  in the Sun neighbourhood (Allen 1976), this means that the star has to be foreground; however, the DSS plate shows an optical cluster just towards IRS 18 which may represent the front end of a larger star aggregate belonging to VMR-D, so the given value is not just a lower limit for the cloud distance. Then, this estimate is in agreement, within the uncertainties and the simplifying assumption of an A0 V star, with the distance to the VMR-D of  $700 \pm 200$  pc given in Paper I.

Throughout the examined fields we have found objects with only a lower limit at  $J$ , hence with either an intrinsic NIR excess and typical colours of Class I sources, or very large extinctions ( $A_V \sim 30 - 40$  mag) if falling within the main sequence reddening band in colour-colour diagrams. Using source # 176 as a test case, we cannot exclude, only on the basis of the  $K$  fluxes, that such objects are heavily obscured background stars. In fact, assuming it is a reddened star, we can estimate an extinction  $A_V \sim 45$  mag from the colour-colour diagram and derive its intrinsic  $V$  magnitude (using the colours given by Koornneef 1983). Then, comparing the obtained value with absolute visual magnitudes of a wide range of spectral types and luminosity classes (Allen 1976), we checked that supergiant stars yielding the same obscured  $K$  flux should be located at

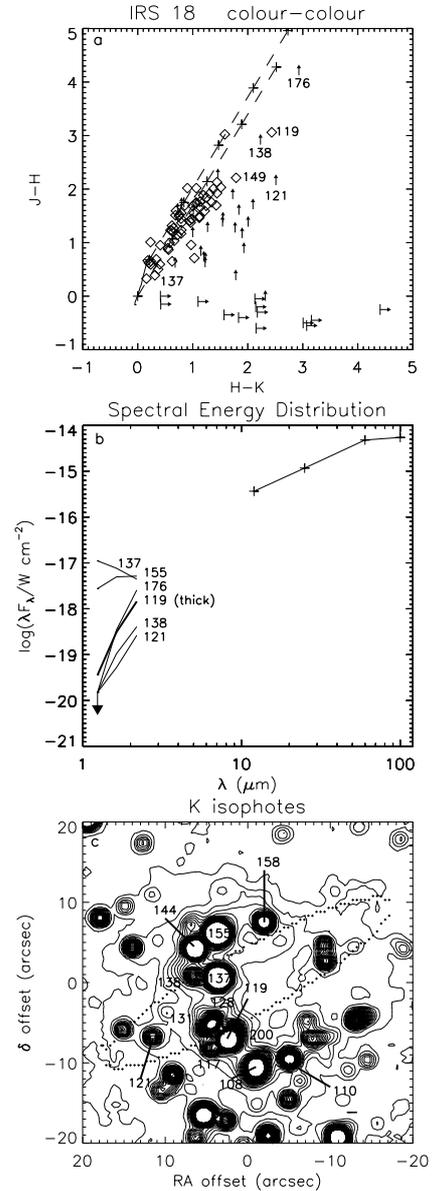
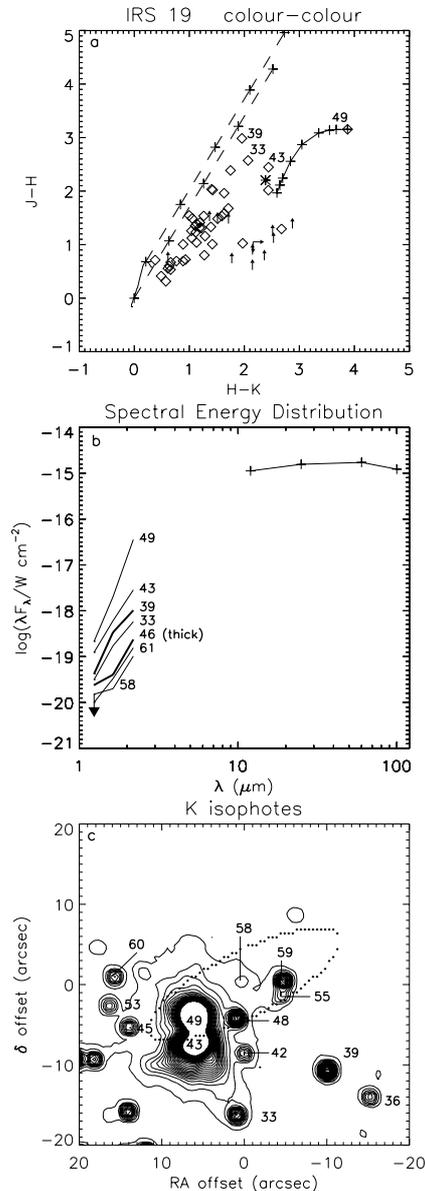


Fig. 6. Same as Fig. 3, but for IRS 18

distances in excess of  $\sim 2000$  pc, well behind the VMR-D cloud. Only small differences arise in terms of extinction from the fact that the locus of supergiant stars does not coincide with the main sequence.

### 3.1.5. IRS 19

The northern part of an extended source, again a possible reflection nebula, is located inside the eastern half of the IRAS uncertainty ellipse. This nebula hosts the brightest point source in the field, # 49, which, as clearly shown in Fig. 7, largely dominates the  $K$  flux and obeys the counterpart criteria. In the  $L'$  image it appears as the most prominent source. Its  $JHK$  magnitudes are also equal, within the errors, to those found through single channel



**Fig. 7.** Same as Fig. 3, but for IRS 19. An asterisk in **a** indicates the colours of the observed nebula, whereas the curved line represents a  $\lambda^{-4}$  scattering law drawn by varying  $\tau_0$  (see Sect. 4.2)

photometry (Paper I), meaning the previous identification is correct. All other sources within or around the ellipse are at least one order of magnitude fainter in the *K* band and have spectral indices less than that of source # 49. Thus, they are unlikely to substantially contribute to the FIR flux. The identification of # 43 (towards the southern part of the nebula; see Fig. 7) as a point source may be questioned and it could just represent the brightest part of the reflection nebula. The colour-colour diagram shows a large number of objects with possible NIR intrinsic excesses, suggesting, also in this field, the presence of a young embedded cluster.

### 3.1.6. IRS 20

Here, the IRAS uncertainty ellipse falls roughly among 3 extended nebulosities (see Fig. 8c), two of them lying within the ellipse, at least partially. The southernmost nebula, whose photometry coincides with the single channel photometry, was previously identified as the NIR counterpart of IRS 20 (Paper I). Yet, as shown in Fig. 8c, this nebulosity is located at the edge of the IRAS ellipse and hosts no star-like objects. In fact, we doubt that sources # 82, # 96 and # 109 are real stellar objects and suspect they correspond to the densest regions in the nebulae. Other sources (# 73 and 74; see Table 4) could be blobs of nebular emission, as well. We think that source # 98, which has the steepest spectral index and is near to the ellipse centre represents the best counterpart candidate. No images in the *L'* band are available. We note that # 93, which however lies  $\sim 46''$  west of the ellipse centre (hence, out of the field depicted in Fig. 8c), also may have the colours of a Class I source (depending on the real value of its *J* brightness, which is a lower limit in magnitudes). Similar argumentations as for IRS 18 suggest that a heavy reddened background star cannot be rejected in this case.

The colour-colour diagram of Fig. 8 shows a high dispersion around the reddening band, but most of the sources located on the left of the band have large error bars, such as a few of those on the right. On the contrary, the sources within the reddening band have well defined colours and display a high degree of extinction. We note also that a number of sources are present with only lower limits at *J* and *H*. Hence, it is quite likely the existence of a young embedded star cluster.

### 3.1.7. IRS 21

The IRAS uncertainty ellipse overlays a group of point sources, and is off-centred towards the south with respect to the latter. The brightest objects of the group (in the *K* band) are located within the ellipse or close to its southern edge (see Fig. 9c), meaning they contribute to the most of the FIR flux. Source # 50, which has a lower limit at *J*, anyway fits the counterpart criteria, although the source previously identified through single channel photometry (see Paper I) is probably # 32. The latter, however, is outside the ellipse, has the colours of a reddened main sequence stars (see Fig. 9a) and has a smaller spectral index with respect to source # 50 (see Fig. 9b). Unfortunately, due to the same arguments as used for IRS 18, we cannot exclude the possibility that # 50 is a very reddened background star.

A contribution from source # 27 must have affected the single channel photometry in the *K* band, since this object is only a few arcsec from # 32. Because of its spectral shape and typical colours of a luminous Class I source, this appears to be a counterpart candidate (see Figs. 9a,b);

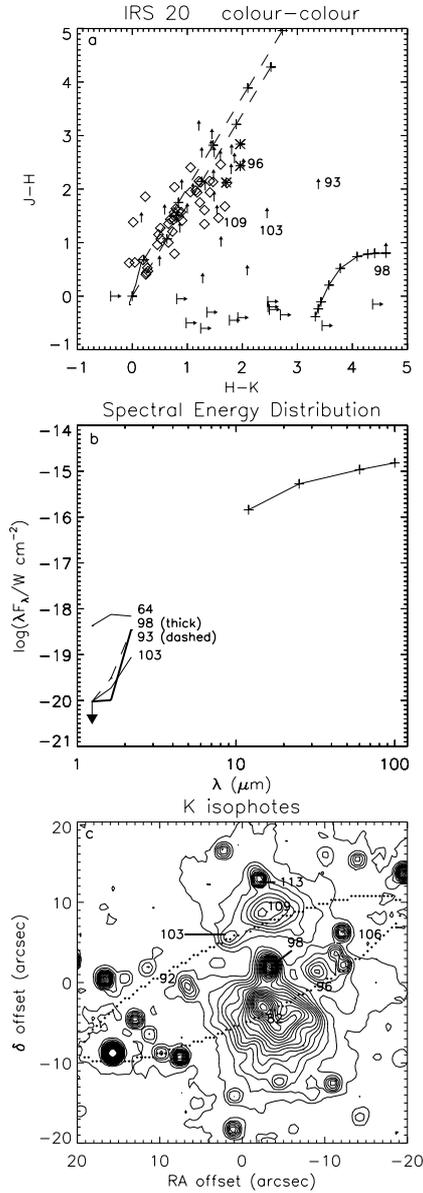


**Fig. 8.** Same as Fig. 3, but for IRS 20. The asterisks in **a**) mark the colours of the observed nebulae, whereas the curved line represents a  $\lambda^{-4}$  scattering law drawn by varying  $\tau_0$  (see Sect. 4.2)

nevertheless, its location with respect to the ellipse may indicate that source # 50 is prominent at FIR wavelengths. Similarly, sources # 47 and # 35, which have the colours of Class I sources, lie to the south or to the south-east of the IRAS uncertainty ellipse. However, they witness again the existence of a young embedded star cluster. No images in the  $L'$  band are available.

### 3.1.8. IRS 62

Figure 10b suggests that source # 27, coinciding with the one already found through single channel photometry (as

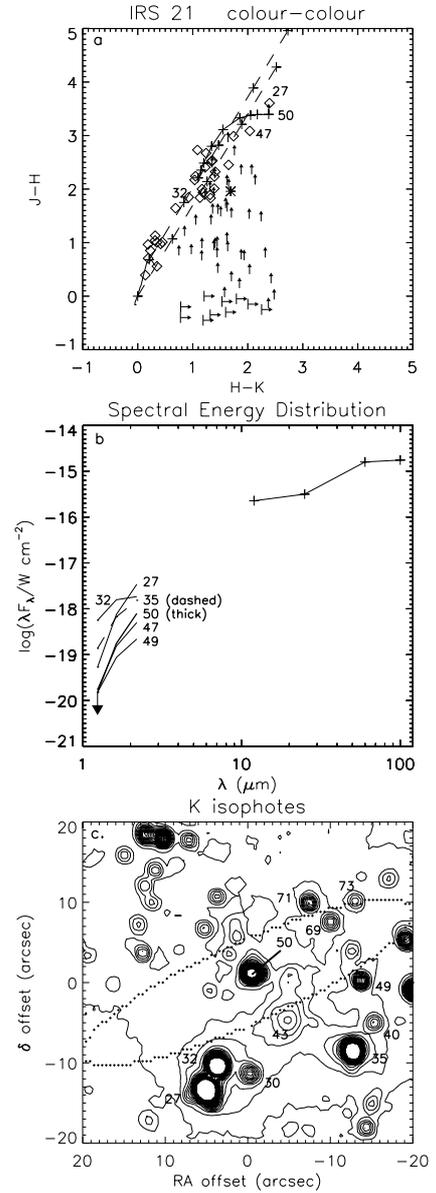


**Fig. 9.** Same as Fig. 3, but for IRS 21. An asterisk in **a**) marks the colours of the observed nebula, whereas the curved line represents a  $\lambda^{-4}$  scattering law drawn by varying  $\tau_0$  (see Sect. 4.2)

indicated by its  $J$ ,  $H$  and  $K$  magnitudes; see Paper II), is a suitable candidate. However, as shown in Fig. 10c, it is clearly outside the IRAS ellipse, so # 26, which is very close to the ellipse centre and has a similar spectral index, may be the real counterpart. Both objects have colours which are typical of luminous Class I sources, yet # 27 displays equal fluxes at  $K$  and  $12 \mu\text{m}$ , so we cannot exclude that it contributes a not negligible part to the FIR flux. Indeed, the IRAS compactness parameter is  $E$  at  $12 \mu\text{m}$  (see Paper II), suggesting a slight deviation from point-likeness at this wavelength. No images in the  $L'$  band are available.

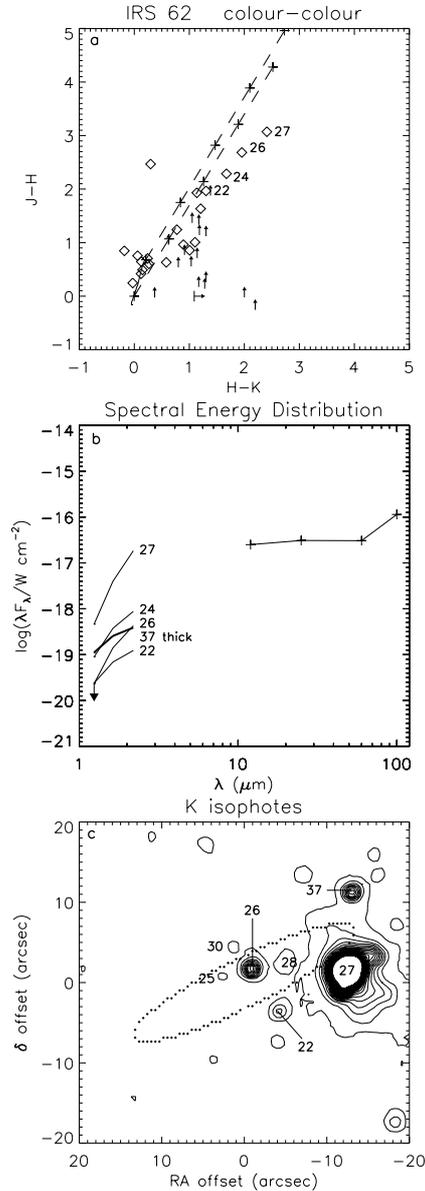


Fig. 10. Same as Fig. 3, but for IRS 62

### 3.1.9. IRS 63

In this case, the IRAS uncertainty ellipse does not include point sources, and clustering, if any, is small. There are only a few objects lying at the edge of the ellipse (see Fig. 11c) and, furthermore, source # 27, which dominates in the  $K$  band and whose  $J$ ,  $H$  and  $K$  magnitudes roughly coincide with those found through single channel photometry, clearly has a negative spectral index (it is also plainly visible in the DSS plate). The reddest objects are # 33, 11 and 21, but these are outside the ellipse. Source # 33 lies about  $20''$  east of the ellipse centre and appears embedded in a faint nebosity (see Fig. 11c), source # 21 is the nearest to the ellipse whereas source # 11 is about  $40''$  south-east of the ellipse centre. The protostellar nature of # 22, an object undetected at  $J$  and  $H$ , is suggested by

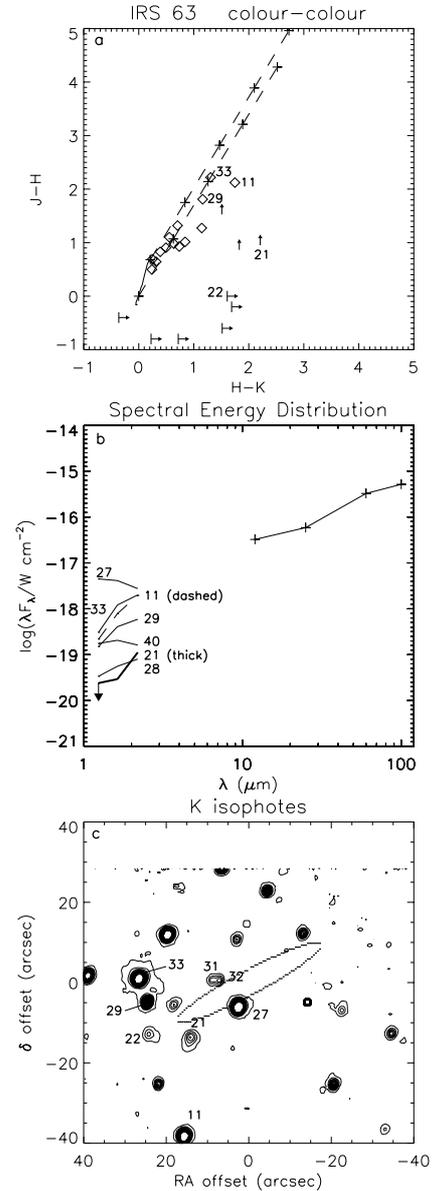


Fig. 11. Same as Fig. 3, but for IRS 63

narrow band NIR images which show  $\text{H}_2 v = 1 - 0 S(1)$  compact emission coinciding with this source (Massi et al. 1997). Although similar argumentations as for IRS 18 can be used in order to show that # 21 could be a heavily reddened background star, given its closeness to the IRAS ellipse and its slightly steeper SED in the NIR, this source appears, at the moment, the best counterpart candidate; an important contribution to the FIR flux may come from sources # 33 and 11, as well. No images in the  $L'$  band are available.

### 3.1.10. IRS 66

As shown in Fig. 12a, source # 31 has typical colours of Class I sources; however, it lies  $\sim 40''$  from the ellipse

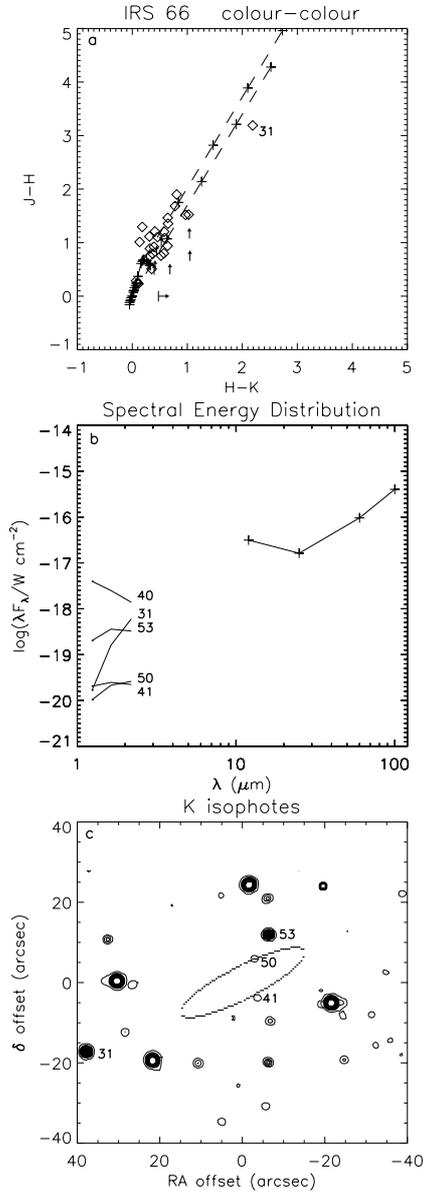


Fig. 12. Same as Fig. 3, but for IRS 66

centre. No other sources fulfil the requirements to be considered as NIR counterparts and, conversely, their colours are compatible with those of reddened main sequence stars. In Paper I (see Appendix) it was speculated that the FIR flux may in part arise from the HII region RCW 32; this could also explain the larger positional error with respect to the IRAS ellipse. Otherwise, the real counterpart should have  $K \geq K_{\text{compl}}$ . No images in the  $L'$  band are available.

### 3.1.11. IRS 67

Source # 61 fulfils the counterpart criteria, and has the colours of a Class I source (as judging from Fig. 13a). Previously, no counterparts had been found within  $K =$

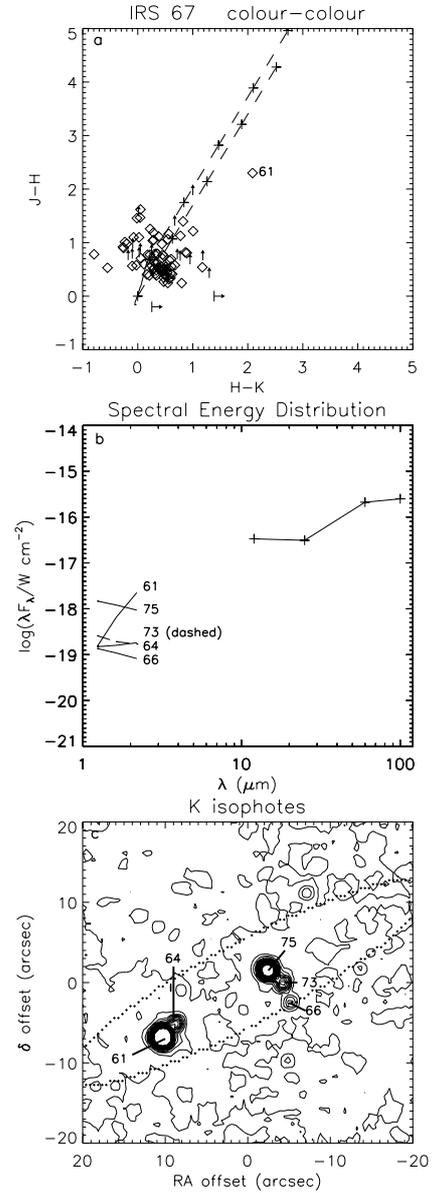


Fig. 13. Same as Fig. 3, but for IRS 67

12.5 mag (see Paper II). All other sources surrounding the IRAS uncertainty ellipse are very faint, in fact most of the points on the left of the main sequence in the colour-colour diagram have large error bars, as a number of point on the right. Nevertheless, some of the NIR excesses on the right appear to be better established, suggesting there may be a few classical T-Tauri stars. No images are available in the  $L'$  band.

### 3.1.12. IRS 71

Source # 66 is located near the center of the uncertainty ellipse, but probably it is # 85, north of the ellipse, that was found through single channel photometry (see Paper II). However, a few objects either show a possible

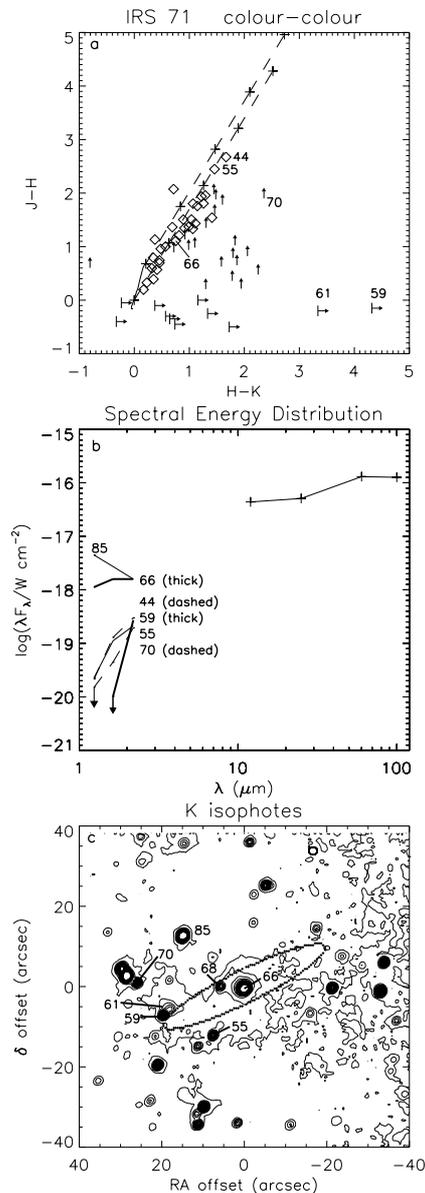


Fig. 14. Same as Fig. 3, but for IRS 71

IR colour excess, or appear as very reddened stars (see Fig. 14a), or have a greater spectral index (see Fig. 14b), namely # 44, 55 and 70. All these sources lie in proximity of the eastern edge of the ellipse, and may contribute to the FIR flux. We note the presence of sources # 59 and 61 at the eastern edge of the ellipse, which are very reddened, remaining undetected in the  $J$  and  $H$  bands: they probably have the greatest spectral index, as shown in Fig. 14b. Thus, # 59, the brightest one, may be the main contributing source to the FIR flux. No images in the  $L'$  band are available.

### 3.2. Comparison with the results of Papers I and II

As seen in the previous section, 4 (out of 10) of the NIR objects indicated as counterparts of IRAS sources in Papers I and II have been confirmed by our NIR data, whereas in 2 fields no suitable candidates had been found. The 4 sources show mean differences between aperture photometry (this paper) and single channel photometry (Papers I and II) of  $K = 0.1$ ,  $H = 0.7$  and  $J = 1.2$  mag, respectively. The greatest differences are for IRS 17 in  $K$  (0.8 mag),  $H$  (1.6 mag), and  $J$  (2.8 mag). These discrepancies are due to both confusion in the  $15''$  beam used in single channel photometry and differences in the sky areas used to estimate the background values. In this sense, single channel photometry and aperture photometry coincide within errors for all these sources.

As for the remaining 6 fields, the identifications given in Papers I and II are wrong and the (possible) NIR counterparts we have found are significantly fainter in all 3 bands with respect to the previous ones. Almost all fields contain one or more objects which, in a colour-colour diagram, fall on the upper right corner, a region typically occupied by Class I sources (Lada & Adams 1992), and this cannot be purely coincidental. Whereas usually one of these red sources dominates in the  $K$  band, excepted towards IRS 63 and IRS 71, there are 3 fields (namely, IRS 21, IRS 62 and IRS 66) in which ambiguities arise since the brightest of the red objects do not lie within the IRAS uncertainty ellipse, and in 2 of these cases fainter sources with NIR excesses do exist much closer to the ellipse centre. One of the IRAS sources, IRS 14, can be classified as a Herbig Ae/Be star rather than a Class I source (see also Appendix).

Only among IRAS sources with  $F_{12} \geq 2.5$  Jy (number codes  $\leq 55$  in our internal classification) we find counterparts with  $K < 10$  mag, whereas IRAS sources with  $1 \leq F_{12} < 2.5$  Jy (number codes  $> 55$ ) tend to have  $K > 10$  mag. However, no clear correlation is evident between IRAS and NIR fluxes, as can be deduced from Table 2, which lists the VMR-D IRAS Class I sources along with their NIR counterparts, sorted according to the  $60 \mu\text{m}$  flux. The coordinates of the NIR counterparts are given in the table, as well; they are hereafter assumed as positions of the newly identified Class I sources.

### 3.3. mm data

The 1.3 mm observations can be used to determine the masses of circumstellar envelopes, since dust emission is likely to be optically thin at this wavelengths. Adopting the formalism of Hildebrand (1983), the total gas mass,  $M_{\text{env}}$ , is given by:

$$M_{\text{env}} = \frac{F_{\nu} \cdot D^2}{k_{\nu} \cdot B_{\nu}(T_d)} \quad (1)$$

**Table 2.** NIR counterparts of the VMR-D IRAS Class I sources. The latter are named according to our internal classification, whereas the former are numbered following Table 4. CC indicates the IRAS compactness parameter (see Paper I). The coordinates of the NIR counterparts are also given

IRAS source	CC	NIR Counterpart (this paper)	$K$ (mag)	$\alpha(1950.0)$			$\delta(1950.0)$			NIR Counterpart (Papers I/II)	
				h	m	s	°	'	"		
IRS 18	952	BAAA	119	12.06	08	47	0.18	-42	43	18.8	different
IRS 19	343	AAAA	49	8.59	08	47	1.83	-43	21	18.6	same
IRS 17	327	AABB	57	9.92	08	44	49.11	-43	43	27.4	same
IRS 21	317	BAAA	50 <sup>a</sup>	12.72	08	47	47.02	-43	59	32.4	different
IRS 20	216	AAAB	98	13.59	08	47	39.02	-43	05	58.6	different
IRS 13	178	AAAA	29	9.06							same
IRS 63	65.20	EAAB	21 <sup>a</sup>	14.84	08	39	24.62	-40	41	31.6	different
IRS 67	42	BBBA	61	11.58	08	44	36.55	-44	20	20.6	none
IRS 14	35.60	AAAA	37	8.58	08	40	27.16	-40	33	21.1	same
IRS 71	26.00	AAAA	59	13.88	08	50	2.96	-42	54	17.9	different
IRS 66	19.20	CCDC	31 <sup>b</sup>	13.01	08	42	57.78	-40	56	1.3	none
IRS 62	6.10	AAAC	26 <sup>a</sup>	13.39	08	32	49.67	-43	14	12.8	different

<sup>a</sup> Tentative identification.

<sup>b</sup> Outside the IRAS uncertainty ellipse.

where  $F_\nu$  is the observed flux density,  $D$  is the distance to the source,  $B_\nu(T_d)$  is the Planck function and  $k_\nu$  is the opacity per unit (gas) mass. Ossenkopf & Henning (1994) discuss the best choice for  $k_\nu$  on theoretical grounds, concluding that a value  $\sim 1 \times (M_{\text{dust}}/M_{\text{gas}}) \text{ cm}^2 \text{ g}^{-1}$ , is likely in dense circumstellar envelopes, which, for a ratio  $M_{\text{dust}}/M_{\text{gas}} = 0.01$ , is greater than the interstellar medium opacity ( $0.0026 \text{ cm}^2 \text{ g}^{-1}$ ), because of grain coagulation and ice mantle growth over them. The envelope masses for the 12 Class I sources have been calculated assuming a dust temperature  $T_d = 30 \text{ K}$  and are listed in Table 3. The uncertainty on  $k_\nu$ , as quoted by Ossenkopf & Henning (1994), should amount to a factor of 2, though an upper limit on  $M_{\text{env}}$  can be set using the interstellar medium dust opacity (yielding masses 5 times greater than indicated in Table 3). Since the telescope was pointed towards the IRAS uncertainty ellipse centres and the beam is roughly comparable with the ellipse sizes, this could result in a flux (i.e., mass) underestimate whenever the identified NIR counterpart lies far from the IRAS uncertainty ellipse centre.

Finally, we can evaluate whether the values derived for the envelope masses are consistent with the central masses derivable from the observed luminosities. The bolometric luminosities obtained by integrating the observed SED's from  $1.25 \mu\text{m}$  ( $J$  band) to  $1.3 \text{ mm}$  are reported in Col. 2 of Table 3, excepted for IRS 71 (because of an upper limit at  $100 \mu\text{m}$ ) and IRS 66 (no millimetric data). These are increased by a factor  $4 \pm 1$  with respect to the values given in Papers I and II. As expected, the bolometric luminosities are dominated by the emission at IRAS and submm wavelengths. In addition, as a consequence of our selection, the luminosities are relatively high ( $120 \leq L/L_\odot$

**Table 3.** Bolometric luminosities and circumstellar envelope masses derived from  $1.3 \text{ mm}$  dust emission

Source	$L_{\text{bol}}$ ( $L_\odot$ )	$M_{\text{env}}$ ( $M_\odot$ )
IRS 62	$1.2 \cdot 10^2$	0.24
IRS 13	$9.6 \cdot 10^2$	2.6
IRS 63	$5.1 \cdot 10^2$	3.1
IRS 14	$2.5 \cdot 10^2$	0.22
IRS 67	$2.6 \cdot 10^2$	0.20
IRS 17	$3.1 \cdot 10^3$	6.4
IRS 18	$5.6 \cdot 10^3$	14.5
IRS 19	$1.6 \cdot 10^3$	3.5
IRS 20	$1.6 \cdot 10^3$	2.2
IRS 21	$1.8 \cdot 10^3$	0.7
IRS 71	-	0.53

$\leq 5600$ ) and probably reflect central masses in the range  $3.5 < M/M_\odot < 10$ , according to the models of Palla & Stahler (1993), i.e. protostellar candidates of intermediate mass. Noting that  $0.2 \leq M_{\text{env}}/M_\odot \leq 15$  (see Table 3), we can conclude that the envelopes seem to have masses which are not a small fraction of that condensed on the central object. This finding indicates these sources might have not yet accumulated most of their stellar mass.

In summary, the NIR images and the  $1.3 \text{ mm}$  photometry allow us to determine coordinates (given in Table 2) and SED's for 11 newly identified Class I objects and a Herbig Ae/Be star.

## 4. Discussion

### 4.1. Clustering

In Papers I and II, SED's were derived for all selected YSO's based on IRAS fluxes (within beams of  $\sim 1'$ ) and single channel NIR photometry (with an aperture of  $15''$ ). These SED's were then used to determine the luminosity function (LF) of Class I sources in the VMR. Yet, source clustering may have affected significantly both SED's and the LF, therefore making compelling to assess the degree of source multiplicity (and extendedness) using NIR images. The way in which clustering may have acted is threefold: first, uncorrect identifications of NIR counterparts may have caused errors in the SED's at NIR wavelengths; second, if FIR fluxes (whose resolution is somewhat low) generally resulted from the contribution of two or more close-by sources, the true LF might differ both in the shape and in the luminosity range. Third, the IRAS Class I sources may "conceal" fainter Class I sources whose presence, anyway, should be accounted for in the LF (*shadowing*).

As for SED's, we found that NIR fluxes need to be revised (downward) in 6 cases (namely, IRS 18, IRS 20, IRS 21, IRS 62, IRS 63 and IRS 71). Yet, previous estimates of the NIR contribution to the bolometric luminosity are  $< 0.5\%$  of the whole emitted energy for all sources but IRS 62, where it amounted to  $17.4\%$  (see Papers I and II). Hence, given that NIR fluxes were found to be  $\gtrsim 10\%$  of the total flux throughout the catalogue of VMR Class I sources (see Table 5 of Paper I and Table 3 of Paper II), and considering that any change due to misidentifications of NIR counterparts is likely downward, these changes barely affect the bolometric luminosities and, hence, the LF.

Instead, it is much more important to check the possibility that IRAS fluxes may result from the contribution of two or more extremely close-by objects. Although clustering is well evident in our images at size scales  $\gtrsim 1' \times 1'$  (see Fig. 2, and our paper in preparation for an in-depth discussion), IRAS Class I sources do seem to have well defined NIR counterparts which begin to dominate the emission in the  $K$  band. Generally, many objects lie within or near the IRAS uncertainty ellipse, but they are well resolved (see, e.g., Fig. 4c), and often much fainter than the Class I source main candidates (see, e.g., Fig. 5c). A few images show in fact that the identified counterparts stand out even more noticeably in the  $L'$  band with respect to all other NIR sources (IRS 13, IRS 14, IRS 17 and IRS 19). However, in some cases (IRS 18, IRS 62, IRS 63) Mid-Infrared observations at comparable spatial resolution are compulsory in order to confirm the predominance of a single source.

Once excluded the possibility that more sources contribute to the IRAS fluxes, shadowing remains the major concern, since in many fields there are more than one

object with typical colours of Class I sources. Some of the "shadowed" sources (i.e., possible Class I sources discarded as IRAS counterparts) have greater  $K$  luminosities with respect to other IRAS counterparts (e.g., IRS 17 # 40 and IRS 13 # 25); unfortunately, it is not possible to infer a bolometric luminosity from the NIR brightness only, since, as we have already shown, there is no correlation between NIR and IRAS fluxes. However, there are indications that these sources, if their protostellar nature was confirmed, have to be accounted for probably only in the  $L \gtrsim 100 L_{\odot}$  part of the LF. In fact, let us first examine the case of IRS 62 # 27: though we have not considered it as the NIR counterpart of the IRAS source, it is one of the NIR brightest Class I (-like) sources we have found. Nevertheless, certainly it has a small bolometric luminosity ( $< 120 L_{\odot}$ ; see Table 3). Similarly, IRS 13 is the less luminous of the IRAS sources with  $F_{12} > 2.5$  Jy (excluding IRS 14) and one of the brightest in the  $K$  band (# 29); in this field, two objects have typical colours of Class I sources (# 25 and 29), but only one seems to dominate in the FIR, so the other cannot affect the upper luminosity end of the LF.

Then, if bright Class I sources are accompanied by other YSO's of the same kind, these latter should have somewhat smaller bolometric luminosities (however, a conclusive assessment in this sense requires Mid-Infrared observations). Therefore, the LF given in Paper II should be well established for  $L \gtrsim 10^2 L_{\odot}$ , unless clustering at a size scale of  $\gtrsim 2''$ , a conservative estimate of the  $K$  image resolution, occurs. Assuming a distance of 700 pc, this would indicate that multiple stars form within 0.007 pc of each others (i.e.,  $\sim 1500$  AU). But this size is roughly less than typical diameters of circumstellar envelopes, so this scenario appears unrealistic. Actually, we cannot rule out the possibility that a few NIR counterparts of the IRAS sources are close binaries; anyway, even in the worst case of companions with the same bolometric luminosity of the main object the inferred *protostar* masses would not be greatly changed. At the high luminosity end, the true LF should not be significantly different from that found by Lorenzetti et al. (1993), if roughly the same fraction of sources in each luminosity bin is composed of close binaries of identical mass. Also a wider mass spectrum for the companions of  $\gtrsim 10 M_{\odot}$  protostars would probably reflect on basically the low luminosity end of the LF. However, this issue cannot be settled by our observations.

### 4.2. Reflection nebulae

Remarkably, we found extended nebulosities in a number of fields; these probably represent reflection nebulae and further confirm the youthness of the objects in the region. The NIR counterparts of 5 IRAS sources (namely IRS 13, IRS 14, IRS 17, IRS 18 and IRS 19) appear embedded in nebulosities. Furthermore, within the fields of

IRS 20, IRS 21 and IRS 62, small nebulae lie close to the IRAS source and, in the remaining fields, the NIR counterparts may be embedded in faint patches of diffuse emission (e.g. IRS 71). The nebulosities are well evident in  $K$  images and, sometimes, less evident in the  $J$  band, because of either the increase in bulk extinction or/and the SED of the illuminating sources (usually extremely red). Note also that the majority of nebulosities (IRS 13, IRS 14, IRS 17, IRS 18, IRS 19 and IRS 62) host multiple stars separated by a few arcseconds from each other.

It is interesting to examine in closer detail the morphology of IRS 20 and IRS 21, where apparently the NIR counterparts are not embedded in the local nebulosities. In IRS 20 (see Fig. 8c) three nebulosities are projected around source # 98; although we have found sources within the diffuse emission (# 82, 96 and 109), they are probably only small nebular peaks. In fact, the colours of sources # 82 and # 96 are very similar to those obtained from the integrated brightnesses of the corresponding nebulae (indicated by asterisks in Fig. 8a), but note that, since these sources are somewhat fainter than the whole nebulae (see Table 4), they do not significantly contribute to the integrated fluxes. Conversely, although the colours of # 109 are quite different from those of the corresponding nebula (see Table 4), morphologically, it resembles a blob of nebular emission rather than a star-like object, as well (Fig. 8c).

As a result, it is tempting to interpret the structure towards IRS 20 as a single reflection nebula illuminated by source # 98, in a region of highly variable extinction, which could make up dark lanes splitting the extended emission into three parts. In this case, the colours of the nebulae must be consistent with those of the illuminating source. To check this circumstance we assume a  $\lambda^{-4}$  dust *isotropic* scattering; hence, the *received* flux from a reflecting nebula is roughly given by:

$$F_\lambda = \frac{f_\lambda \Omega_s L_0(\lambda)}{4\pi d^2} \left[ 1 - \exp\left(-\frac{\tau_0}{\lambda^4}\right) \right] \quad (2)$$

where  $L_0(\lambda)$  is the luminosity of the illuminating source in the  $\lambda$  band,  $f_\lambda$  a factor accounting for atmospheric transmission, filter bandpass and detector sensitivity,  $\Omega_s$  the fraction of solid angle subtended by the nebula (with respect to the illuminating source),  $d$  the distance from the observer,  $\lambda$  the effective wavelength and  $\tau_0$  a factor depending on the density and geometry of the nebula. Assuming  $\tau_0$  does not depend on  $\lambda$ , the colour of a reflection nebula is given by:

$$m_{\lambda_2} - m_{\lambda_1} = -2.5 \log \left[ \frac{f_{\lambda_2} L_0(\lambda_2)}{f_{\lambda_1} L_0(\lambda_1)} \right] - 2.5 \log \left[ \frac{1 - \exp\left(-\frac{\tau_0}{\lambda_2^4}\right)}{1 - \exp\left(-\frac{\tau_0}{\lambda_1^4}\right)} \right] \quad (3)$$

where  $m_\lambda$  is the flux in magnitudes and we have considered no extinction. Note that the first term on the right-hand side is the intrinsic colour of the illuminating source.

The isotropic scattering law (applied to # 98) has been drawn in Fig. 8a by varying  $\tau_0$ ; both the illuminating source and the reflection nebulae must be individually reddened according to the extinction towards them. Since the brightest nebula exceeds in  $K$  luminosity # 98 by 3 mag, the extinction  $A_V$  towards # 98 must be at least  $\sim 30$  mag greater than towards the nebula (assuming  $A_K = 0.11 A_V$ ; see Rieke & Lebofsky 1985), if the former illuminates the latter (since a reflection nebula cannot be intrinsically brighter than its illuminating source). As indicated in the colour-colour diagram of Fig. 8a (where, as said, nebulae are indicated by asterisks), the given value of  $J - H$  for source # 98 is a lower limit, suggesting that # 98 might have a sufficiently large  $J - H$  to account both for the colours and for the  $K$  flux difference of the nebulae. Namely, the position of # 98 in Fig. 8a is allowed to be moved in the upper right corner of the plot in such a way that the scattering law is compatible with the obscured colours of the nebula, once the extinction is accounted for. Similarly, it is possible to find combinations of  $\tau_0$ ,  $\Omega_s$  and extinction which account for both colours and  $K$  flux differences of the three individual nebulae. Other star-like objects close to the smallest nebulae (# 113, 96, 99, 102) cannot account for the nebular colours since lying to the left in the colour-colour diagram, with the possible exception of # 103.

A small extended nebulosity (source # 43) appears to the south of the NIR counterpart (source # 50) of IRS 21 (see Fig. 9c). The isotropic scattering law (applied to # 50) has been drawn in Fig. 9a and, as can be seen, the colours of # 43 are, in principle, compatible with those of a reflection nebula illuminated by # 50, if the latter is more extinguished than the former of  $A_V \sim 12$  mag (according to the colour-colour diagram of Fig. 9a, where the nebula is indicated by the asterisk). Source # 43 is as bright as source # 50 in the  $K$  band, so, considering an extinction difference between the object and the nebula  $A_K \sim 0.11 \times 12 = 1.3$  mag, it would be  $\sim 1.3$  mag fainter, whereas its small apparent size would indicate a difference of at least  $K = -2.5 \log(\Omega_s) \sim 2.0$  mag, in rough agreement considering the oversimplification of our model. In conclusion, both in the case of IRS 20 and IRS 21 the NIR counterparts of the IRAS objects may be the illuminating sources of nearby nebulosities.

As shown in Fig. 7a, also the colours of the nebular emission (indicated by the asterisk) south of source # 49, towards IRS 19, are compatible with isotropic scattering of NIR radiation from # 49 itself. It must be more extinguished than the nebula, since it is  $\sim 1$  mag fainter in the  $J$  band; this means  $A_V > 3.5$  mag (using the reddening law of Rieke & Lebofsky 1985) which is plausible as can be checked in the colour-colour diagram of Fig. 7a. Conversely, the colours of # 43 (an object found within

the nebula) are very similar to those obtained from the integrated magnitudes of the nebula itself, but since it is much fainter than the latter, # 43 is probably only part of the nebular emission.

In conclusion, if the NIR counterparts of IRS 19, 20 and 21 are the illuminating sources of the nearby nebulosities, they must be heavily extinguished (more than  $A_V \sim 30$  mag in one case), confirming their nature of embedded Class I sources.

The large number of (possible) reflection nebulae is not unexpected; e.g., Yun et al. (1994) found evidence of embedded nebulosities in 11 out of 34 Bok globules imaged in the *JHK* bands. Nebulae which appear brighter in the *K* band than in the *J* band are found by these authors to be associated with IRAS sources displaying a  $12/25 \mu\text{m}$  spectral index  $\alpha = d \log(\nu B_\nu) / d \log \nu < 0$ , and are attributed to objects deeply embedded in the clouds. According to these authors, they represent an earlier evolutionary state with respect to similar regions associated with nebulae which are brighter in the *J* band. According to our observations, most of the Class I source candidates in VMR-D would be in this stage.

## 5. Conclusions

We have presented *JHK* images along with NIR and 1.3 mm photometry of 11 Class I sources and a possible Herbig Ae/Be star in the Vela Molecular Ridge D cloud, previously identified by Liseau et al. (1992) and Lorenzetti et al. (1993). Whereas clustering of YSO's will be discussed in a forthcoming paper, we have established the following points:

- 1 Through NIR- and mm-photometry, we have determined the SED's for the 11 newly discovered Class I sources (and the Herbig Ae/Be star). Bolometric luminosities range between 120 and  $5600 L_\odot$ , indicating protostars with masses between  $3.5 - 10 M_\odot$ .
- 2 The mm-photometry allows also to derive envelope masses ranging between  $0.2 - 15 M_\odot$ , hence of the same order of the protostar masses deduced above.
- 3 Although clustering is well evident, the NIR counterparts of the IRAS sources seem to be single objects (or, possibly, close binaries), though quite often there is more than one source per field with *JHK* colours typical of Class I.
- 4 The NIR images confirm that 11 IRAS sources are real Class I objects; in the case of IRS 14, we found more appropriate to identify it as a Herbig Ae/Be star.
- 5 Only 4 of the previously identified counterparts through single channel photometry, have been confirmed by the present observations. The NIR contribution to the SED's of the IRAS Class I source candidates must be furtherly revised downward with respect to previous determinations and appears to be  $< 10\%$ .
- 6 Many sources are associated to diffuse emission; 5 NIR counterparts appear embedded in reflection nebulae, whereas 2 NIR counterparts are close to nebulosities (and are probably illuminating them). A bright nebula has been found near the IRAS uncertainty ellipse in one field (IRS 62), possibly unrelated to the NIR counterpart. This frequent association with nebulosities confirms the youthfulness of the targeted objects.
- 7 In IRS 19, IRS 20 and IRS 21, the identified Class I sources may represent the illuminating sources for the observed nebulae. This occurrence implies high values of the extinction towards them (more than  $A_V \sim 30$  mag in one case).

## Appendix A: Data reduction and photometry

The 12 observed fields were imaged in 3 dithered positions each band, namely *A*, *B* and *C*. From these, 3 sky subtracted frames were obtained performing *B-A*, *B-C* and *C-A*, and were divided by a normalized flat field differentially generated (so as to remove any bias) by illuminating a dome screen at two different levels of light intensity. The images were subsequently cleaned for the presence of bad pixels by interpolating across them, and finally registered and co-added, using thresholding and median filtering in order to remove any signal below the sky level introduced by the subtraction, providing a single frame suitable for photometric analysis.

We used the DAOFIND task (Stetson 1987) to identify point sources down to a  $4\sigma$  level; subsequently, each frame was visually inspected at different contrast levels in order to remove false detection or add faint sources undetected by DAOFIND. Then, aperture photometry was performed using PHOT routines with an aperture radius of 2 pixels (about the FWHM of PSF's); this low value was needed in order to accurately measure source brightness in the most crowded areas of the imaged fields, but we checked that it was appropriate for relatively isolated stars as well. Due to the extremely variable background, the sky was sampled in 10-pixel wide annuli centred on each star, with inner radii of 10 pixels. An aperture correction was estimated using the brightest and most isolated stars in each image. The standard deviation of magnitude corrections both within a frame and within a band is generally  $\lesssim 0.1$  mag. The small annulus we have been forced to use because of crowdedness and sky variations, obviously introduces a systematic error in the given *JHK* magnitudes (which, however, we estimate  $\lesssim 0.1$  mag), but we expect that this is severely reduced, at least at the first order, when colours are derived. The *modal value* of pixels within each annulus was chosen for background subtraction; since the sky is extremely variable where also crowdedness is important, the modal value may not adequately sample it; however, we expect that this error may become dominant only for the faintest objects.

**Table 4.** *JHK* photometry and positions of found *K* sources towards IRS 63, given as an example of the whole list in electronic form. Due to the presence of bad pixels or the closeness to the image edge, a few *JHK* entries are not given and marked as “unav” (unavailable)

NIR source	RA(1950) ( <sup>h</sup> <sup>m</sup> <sup>s</sup> )	$\delta$ (1950) ( <sup>°</sup> <sup>'</sup> <sup>''</sup> )	<i>J</i>	<i>H</i> (mag)	<i>K</i>
<b>IRS 63 (08<sup>h</sup> 39<sup>m</sup> 23<sup>s</sup>.4 -40° 41' 18'')</b>					
1	8 39 19.46	-40 42 26.2	unav	unav	unav
2	8 39 19.58	-40 42 24.7	> 18	18.41 ± 0.56	16.87 ± 0.18
3	8 39 22.43	-40 42 21.7	> 18	16.93 ± 0.15	15.90 ± 0.07
4	8 39 24.36	-40 42 20.4	12.90 ± 0.00	12.39 ± 0.00	12.34 ± 0.00
5	8 39 27.22	-40 42 17.7	> 18	> 17	16.88 ± 0.17
6	8 39 29.69	-40 42 14.8	unav	unav	unav
7	8 39 24.85	-40 42 2.7	> 18	> 17	17.57 ± 0.33
8	8 39 20.00	-40 42 2.4	16.71 ± 0.05	15.57 ± 0.04	15.06 ± 0.04
9	8 39 27.53	-40 41 58.9	> 18	16.47 ± 0.08	14.96 ± 0.03
10	8 39 28.55	-40 41 58.3	> 18	17.52 ± 0.22	16.97 ± 0.18
11	8 39 24.75	-40 41 57.0	15.60 ± 0.02	13.48 ± 0.00	11.73 ± 0.00
12	8 39 19.11	-40 41 55.7	17.84 ± 0.12	16.02 ± 0.06	15.19 ± 0.04
13	8 39 20.37	-40 41 54.8	16.69 ± 0.05	16.03 ± 0.06	16.02 ± 0.09
14	8 39 29.35	-40 41 54.3	18.10 ± 0.19	16.99 ± 0.18	16.43 ± 0.13
15	8 39 29.69	-40 41 53.7	unav	unav	unav
16	8 39 25.32	-40 41 43.7	15.28 ± 0.01	14.79 ± 0.02	14.55 ± 0.02
17	8 39 21.49	-40 41 43.4	15.82 ± 0.02	14.84 ± 0.02	14.20 ± 0.01
18	8 39 19.19	-40 41 37.9	> 18	17.52 ± 0.26	16.21 ± 0.10
19	8 39 18.62	-40 41 36.0	18.05 ± 0.15	16.47 ± 0.10	15.69 ± 0.05
20	8 39 18.73	-40 41 33.1	13.60 ± 0.00	13.23 ± 0.00	13.12 ± 0.00
21	8 39 24.62	-40 41 31.6	> 18	17.05 ± 0.14	14.84 ± 0.03
22	8 39 25.54	-40 41 30.9	> 18	> 17	15.39 ± 0.04
23	8 39 20.23	-40 41 30.2	15.67 ± 0.02	15.11 ± 0.02	14.82 ± 0.03
24	8 39 29.65	-40 41 26.8	> 18	unav	unav
25	8 39 19.43	-40 41 24.6	> 18	17.84 ± 0.28	17.21 ± 0.24
26	8 39 21.32	-40 41 24.3	> 18	16.82 ± 0.11	15.47 ± 0.04
27	8 39 23.57	-40 41 23.7	12.32 ± 0.00	11.68 ± 0.00	11.37 ± 0.00
28	8 39 24.99	-40 41 23.2	17.63 ± 0.12	16.35 ± 0.08	15.21 ± 0.04
29	8 39 25.57	-40 41 22.6	16.01 ± 0.03	14.20 ± 0.01	13.03 ± 0.01
30	8 39 27.77	-40 41 21.0	> 18	17.14 ± 0.16	15.31 ± 0.04
31	8 39 24.15	-40 41 16.9	> 18	> 17	15.31 ± 0.04
32	8 39 23.99	-40 41 16.9	16.70 ± 0.05	15.77 ± 0.05	15.04 ± 0.03
33	8 39 25.75	-40 41 16.7	15.23 ± 0.01	13.02 ± 0.00	11.71 ± 0.00
34	8 39 26.86	-40 41 15.9	13.32 ± 0.00	12.63 ± 0.00	12.38 ± 0.00
35	8 39 28.63	-40 41 12.4	17.36 ± 0.09	15.81 ± 0.05	15.30 ± 0.04
36	8 39 29.28	-40 41 10.9	18.38 ± 0.24	15.70 ± 0.06	14.22 ± 0.02
37	8 39 29.69	-40 41 8.7	> 18	17.28 ± 0.22	unav
38	8 39 23.62	-40 41 6.4	16.81 ± 0.05	15.80 ± 0.04	14.95 ± 0.03
39	8 39 25.13	-40 41 5.4	13.39 ± 0.00	12.29 ± 0.00	11.73 ± 0.00
40	8 39 22.17	-40 41 4.7	15.84 ± 0.02	14.94 ± 0.02	14.44 ± 0.02
41	8 39 27.15	-40 41 2.1	14.15 ± 0.00	13.32 ± 0.00	12.93 ± 0.00
42	8 39 27.63	-40 40 56.4	> 18	17.76 ± 0.29	16.46 ± 0.12
43	8 39 22.70	-40 40 56.1	> 18	> 17	17.36 ± 0.25
44	8 39 22.96	-40 40 53.9	15.88 ± 0.02	14.56 ± 0.01	13.85 ± 0.01
45	8 39 28.67	-40 40 49.8	> 18	16.92 ± 0.13	16.30 ± 0.09
46	8 39 22.62	-40 40 48.5	unav	unav	unav
47	8 39 24.66	-40 41 33.0	> 18	> 17	15.48 ± 0.05
48	8 39 25.37	-40 41 31.3	> 18	> 17	16.28 ± 0.10
49	8 39 24.89	-40 41 21.7	> 18	> 17	16.77 ± 0.18

## Appendix B: Notes to individual sources

A short description of the field around each IRAS source is reported in Papers I and II. Here we provide additional information found in the more recent literature:

- IRS 63 - 6.7 GHz methanol maser emission has been searched for without result (limiting flux  $\sim 5$  Jy; Van der Walt et al. 1996). It is an IRAS PSC associated with a bright-rimmed cloud found near an OB association (Sugitani & Ogura 1994).
- IRS 13 - CS (2-1): ( $T_{\text{mb}} = 1.33$  K;  $v_{\text{LSR}} = +9.5$  km s $^{-1}$ ;  $\Delta v = 1.9$  km s $^{-1}$ ; Bronfman et al. 1996). 6.7 GHz methanol maser emission has been searched for with negative results (limiting flux  $\sim 5$  Jy; Van der Walt et al. 1995).
- IRS 14 - It coincides with the sources PRH $\alpha$  161/162 (Pettersson & Reipurth 1994). This source has been classified as a Herbig Ae/Be star by Thé et al. (1994) and, as such, the properties of its circumstellar envelope have been investigated by Pezzuto et al. (1997).
- IRS 17 - Water and 6.6 GHz methanol masers were searched for (Scalise Jr. et al. 1989; Schutte et al. 1993). CS (2-1): ( $T_{\text{mb}} = 5.28$  K;  $v_{\text{LSR}} = +3.7$  km s $^{-1}$ ;  $\Delta v = 4.3$  km s $^{-1}$ ; Bronfman et al. 1996).
- IRS 18 - A 6.6 GHz methanol maser was detected at +11, +15 km s $^{-1}$  (Schutte et al. 1993).
- IRS 19 - Selected as planetary nebula candidate and not detected at 6 cm (rms  $\sim 1$  mJy; Van de Steene & Pottasch 1993). CS (2-1): ( $T_{\text{mb}} = 5.80$  K;  $v_{\text{LSR}} = +12.0$  km s $^{-1}$ ;  $\Delta v = 2.9$  km s $^{-1}$ ; Bronfman et al. 1996).
- IRS 20 - CS (2-1): ( $T_{\text{mb}} = 1.01$  K;  $v_{\text{LSR}} = +2.1$  km s $^{-1}$ ;  $\Delta v = 2.3$  km s $^{-1}$ ; Bronfman et al. 1996). 6.7 GHz methanol maser emission has been searched for with negative results (limiting flux  $\sim 5$  Jy; Van der Walt et al. 1995).
- IRS 71 - A possible H $\alpha$  star has been detected at (19.8, 18) arcsec with respect to the IRAS position (Marquez-Limon et al. 1992 - their # 29). It coincides with our # 85, a source which lies slightly below the reddening line of A0 V stars in the colour-colour diagram and exhibits a relatively small reddening ( $A_V \sim 2$ ).

## References

- Allen C.W., 1976, *Astrophysical Quantities* (3rd ed.). Athlone press, London
- Bouchet P., Moneti A., Slezak E., Le Bertre T., Manfroid J., 1989, *A&AS* 80, 379
- Bronfman L., Nyman L.A., May J., 1996, *A&AS* 115, 81
- Hildebrand R.H., 1983, *QJRAS* 24, 267
- Koornneef J., 1983, *A&A* 128, 84
- Kreysa E., 1990, *Sub-mm Direct Photometry with Large Telescopes*. In: *From Ground-Based to Space-Born Submm Astronomy*. Proc. of the 29th Liege Symp. 3-5 July 1990, ESA SP-314, p. 265
- Lada C.J., Adams F.C., 1992, *ApJ* 393, 278
- Liseau R., Lorenzetti D., Nisini B., Spinoglio L., Moneti A., 1992, *A&A* 265, 577 (Paper I)
- Lorenzetti D., Spinoglio L., Liseau R., 1993, *A&A* 275, 489 (Paper II)
- Marquez-Limon A., Lopez-Molina M.G., Chavarria-K.C., 1992, *A&AS* 95, 391
- Massi F., Lorenzetti D., Vitali F., 1997, *Near Infrared H<sub>2</sub> Imaging of YSOs in Vela Molecular Clouds*. In: Malbet F., Castets A. (eds.) *Poster Proc. IAU Symp. 182, Low Mass Star Formation - from Infall to Outflow*. Observatoire de Grenoble, Grenoble, p. 21
- May J., Murphy D.C., Thaddeus P., 1988, *A&AS* 73, 51
- Moorwood A., Finger G., Biereichel P., et al., 1992, *ESO Messenger* 69, 61
- Murphy D.C., May J., 1991, *A&A* 247, 202
- Ossenkopf V., Henning Th., 1994, *A&A* 291, 943
- Palla F., Stahler S.W., 1993, *ApJ* 418, 414
- Pettersson B., Reipurth B., 1994, *A&AS* 104, 233
- Pezzuto S., Strafella F., Lorenzetti D., 1997, *ApJ* 485, 290
- Rieke G.H., Lebofsky M.J., 1985, *ApJ* 288, 618
- Scalise Jr.E., Rodriguez L.F., Mendoza-Torres E., 1989, *A&A* 221, 105
- Schutte A.J., Van der Walt D.J., Gaylard M.J., MacLeod G.C., 1993, *MNRAS* 261, 783
- Stetson P.B., 1987, *PASP* 99, 191
- Sugitani K., Ogura K., 1994, *ApJS* 92, 163
- Thé P.S., de Winter D., Pérez M.R., 1994, *A&AS* 104, 315
- Van der Walt D.J., Gaylard M.J., Macleod G.C., 1995, *A&AS* 110, 81
- Van der Walt D.J., Retief S.J.P., Gaylard M.J., Macleod G.C., 1996, *MNRAS* 282, 1085
- Van de Steene G.C.M., Pottasch S.R., 1993, *A&A* 274, 895
- West R.M., 1980, *A&A* 90, 366
- Yun J.L., Clemens D.P., 1994, *AJ* 108, 612